Article

Not peer-reviewed version

Flexible and Electrically Conductive 3D Printed MXene-Hydrogel Copolymers for High Precision Sensing of Biomechanical Processes

Tao Huang , Nengqi Xu , Yanan Huang , Shudi Mao , Eman Alghamdi , Qiang Fu , Bing Sun , Charlene J. Lobo * , Xiaoxue Xu *

Posted Date: 6 January 2026

doi: 10.20944/preprints202601.0261.v1

Keywords: direct light processing; biomechanical sensor; MXene composite; additive manufacturing; hydrogel copolymer

 doi:10.20944/preprints202601.0261.v1

Article

Flexible and Electrically Conductive 3D Printed MXene-Hydrogel Copolymers for High Precision Sensing of Biomechanical Processes

Tao Huang [1], Nengqi Xu [2], Yanan Huang [1,2], Shudi Mao [3], Eman Alghamdi [2], Qiang Fu [4], Bing Sun [1], Charlene J. Lobo [1,*] and Xiaoxue Xu [3,*]

[1] School of Mathematical and Physical Sciences, University of Technology Sydney, NSW 2007, Australia.
[2] School of Chemistry and Chemical Engineering, Jiangsu University, Zhenjiang 212013, P. R. China.
[3] School of Biomedical Engineering, University of Technology Sydney, Ultimo, NSW, 2007, Australia.
[4] School of Civil and Environmental Engineering, University of Technology Sydney, Ultimo, NSW, 2007, Australia.
* Correspondence: charlene.lobo@uts.edu.au (C.J.L.); xiaoxuehelen.xu@uts.edu.au (X.X.)

Abstract

Application of MXene-polymer composites in wearable and implantable medical devices requires the development of hydrophilic and biocompatible MXene-polymer hydrogel composites with high electromechanical response, flexibility, and durability. Here, we formulate low weight percentage MXene-hydrogel copolymer inks enabling direct light printing (DLP) of MXene-polyvinyl alcohol (PVA)-polyacrylic acid (PAA)-hydrogel composites. The low wt% MXene-PVA-PAA composites demonstrate high biocompatibility, mechanical flexibility, high sensitivity and high precision for sensing acute bending angles. The sub-millidegree angle resolution and sub-microradian stability of these electromechanical sensors demonstrates their suitability for applications such as high precision tracking of joint movements. In addition, the synthesized MXene membranes show promise for applications in osmotic energy conversion, with a harvested electric power density of 6.79 Wm^{-2}.

Keywords: direct light processing; biomechanical sensor; MXene composite; additive manufacturing; hydrogel copolymer

1. Introduction

Lightweight and biocompatible MXene composite membranes and films have applications in numerous energy storage/generation and biomedical technologies including osmotic energy conversion devices[1], tissue engineering[2], biodegradable microrobots[3] and conformable 3D electronic devices[4]. MXenes are a class of two-dimensional materials similar to graphene, which consist of atomically thin layers of transition metal carbides, nitrides or carbonitrides. The majority of M-X bonds in the two-dimensional sheets are exceptionally strong, while their surfaces can be functionalized with a wide variety of ligands, imparting them with high strength, flexibility, electrical conductivity and thermal stability. Since the discovery of the first MXene $Ti_3C_2T_x$ in 2011, more than 30 other MXenes have been synthesized and extensively characterized[5].

MXene sheets are fabricated by etching MAX phase ceramics, a class of ternary carbo-nitride compounds comprised of a transition metal (M), a group III or IVa element (A), with X representing carbon or nitrogen. The M-A bonds in MAX phases are very strong and resistant to mechanical exfoliation, so production of two-dimensional MX sheets must be done using aggressive acids such as hydrofluoric acid (HF). Once the MX sheets have been exfoliated, they can be intercalated using lithium (Li) ions to delaminate and separate them from the substrate and from each other. This step is often done in an electrochemical cell, or by using molten salts, and is assisted by employing highly mobile Li atoms to separate the MX sheets in a process known as Li intercalation which is also

 doi:10.20944/preprints202601.0261.v1

employed in manufacture of Li ion batteries. The resulting MXenes have chemical formula $M_{n+1}X_nT_x$, where n=1-5 and the T refers to the terminating surface groups (predominantly F^-, O^{2-} and OH^-) produced by the etch process. These surface groups can be functionalized with various ligands (eg. -Cl, and $-NH_3$) in subsequent etching steps.

Combining MXenes with polymer hydrogels such as polyacrylamide, polyvinyl alcohol (PVA) and polyacrylic acid (PAA) enables the development of composites with a unique combination of properties: electrical conductivity imparted by the MXene, and flexibility, biocompatibility and high cell adhesion imparted by the hydrophilic (co)polymer matrix. One of the particularly promising applications of MXene-polymer composites is in wearable and implantable medical devices powered solely by the biomechanical energy generated by physiological processes such as breathing, heart beating, muscle stretching, blood flow and the flow of ions in and out of cells via ion channels[6]. However, to withstand long-term *in vivo* use, implantable MXene devices also require durability under many cycles of repeated stress/strain, and high electrical conductivity to enable readout of electrical signals. These requirements can potentially be met by developing composites combining MXenes such as $Ti_3C_2T_x$ nanosheets with hydrogel polymers such as PVA, PAA and PVA-PAA copolymer blends.

Extrusion-based 3D printing techniques such as Direct ink writing (DIW)[7] and Direct Light Processing (DLP) have recently emerged as promising methods for fabricating MXene composite films with a range of microstructures and morphologies. In DLP, the laser-printed polymers are cured with UV light to complete polymer cross-linking. These techniques require the formulation of inks that have high viscoelasticity and good shear-thinning effect when passing through a small nozzle. There are few commercial inks with these properties, hence development of new inks is an active area of research. Recent work has demonstrated the formulation of a supra-molecular system for DIW which enabled 3D printing of piezoresistive sensors for real-time monitoring of human movement[8]. Emulsion-based graphene oxide and MXene inks have also been developed for 3D printing of foams with high electrical conductivity and electromagnetic shielding performance[9]. Capillary-driven DIW and fused deposition modeling methods have been employed for 3D and 4D printing of MXene nanostructures into ordered arrays and micropatterns on flexible substrates[10,11]. However, so far, there is a lack of hydrophilic and biocompatible MXene inks suitable for 3D DLP, which are necessary for the development of implantable biomedical devices for accurate monitoring of biomechanical processes such as joint movements.

2. Materials and Methods

2.1. Chemicals and Agents

All chemicals were purchased from commercially available sources and used as received. Lithium Fluoride (LiF), Titanium Aluminium Carbide MAX phase (Ti_3AlC_2), n-butyllithium solution 2.5M in hexane, hydrochloride acid (37v% HCl), Poly(vinyl alcohol) (PVA, MW = 89000-98000 g mol^{-1}), acrylic acid (AA, 99 wt% in DI water), poly(ethylene glycol) diacrylate (PEGDA, average M_n = 575 g mol^{-1}), lithium phenyl-2,4,6-trimethylbenzoylphosphinate (LAP) were all purchased from Sigma-Aldrich Australia.

2.2. Preparation of MXene ($Ti_3C_2T_x$) Nanosheets

$Ti_3C_2T_x$ nanosheets were synthesized by etching the Ti_3AlC_2 phase with LiF/HCl as reported previously[12]. Briefly, 1g of LiF powder was dissolved in 20mL of 9M HCl, and the solution was mixed thoroughly at room temperature with rigorous stirring. Then 1g Ti_3AlC_2 was added carefully into the mixed solution drop by drop to avoid overheating from the exothermic reaction. The reaction was allowed to proceed under continuous stirring for 24h at 35 C. The as-obtained precipitate was collected by centrifuging and then washed repeatedly using deionized water until almost neutral pH (6). The solid sample was collected after it was dried at room temperature.

 doi:10.20944/preprints202601.0261.v1

2.3. Preparation of MXene-Hydrogel Copolymer Inks for 3D Printing

MXene-PVA-PAA inks of with MXene concentrations ranging from 0.07-0.28 wt% were prepared by solution blending[13] using water as the solvent. The compositions of each sample are listed in Table 1. The method of formulation of an ink containing 0.28 wt% MXene (denoted by 10PVA25PAA-0.28MXene) is selected as an example of the preparation process. First, 3 g of PVA powder was dissolved in 100 mL of deionized (DI) water at 90 °C for 5 hours to create a 20 wt% PVA solution. Additionally, 30 mg of MXene powder was dispersed uniformly in 15 mL of DI water through sonication under a nitrogen atmosphere for 90 minutes, yielding a 2 mg mL^{-1} MXene solution. Then, 15 mL of the PVA solution and 15 mL of the MXene solution were combined in a light-shielded container. Subsequently, 7.5 g of AA, 75 mg of PEGDA, and 60 mg of LAP were added. The mixture was stirred at 2000 rpm for 5 minutes to prepare the final 3D printing ink, referred to as 10PVA25PAA-0.28MXene in Table 1.

Table 1. Composition of MXene-hydrogel copolymer inks used for 3D DLP.

Sample name	Sample composition	PVA	AA	PEGDA	MXene	LAP	H_2O
PVA-PAA-0.28MX	10PVA25PAA-0.28MXene	3 g	7.5 g	75 mg	30 mg	60 mg	30 g
PVA-PAA-0.14MX	10PVA25PAA-0.14MXene	3 g	7.5 g	75 mg	15 mg	60 mg	30 g
PVA-PAA-0.07MX	10PVA25PAA-0.07MXene	3 g	7.5 g	75 mg	7.5 mg	60 mg	30 g
PVA-PAA	10PVA25PAA	3 g	7.5 g	75 mg	3.75 mg	60 mg	30 g

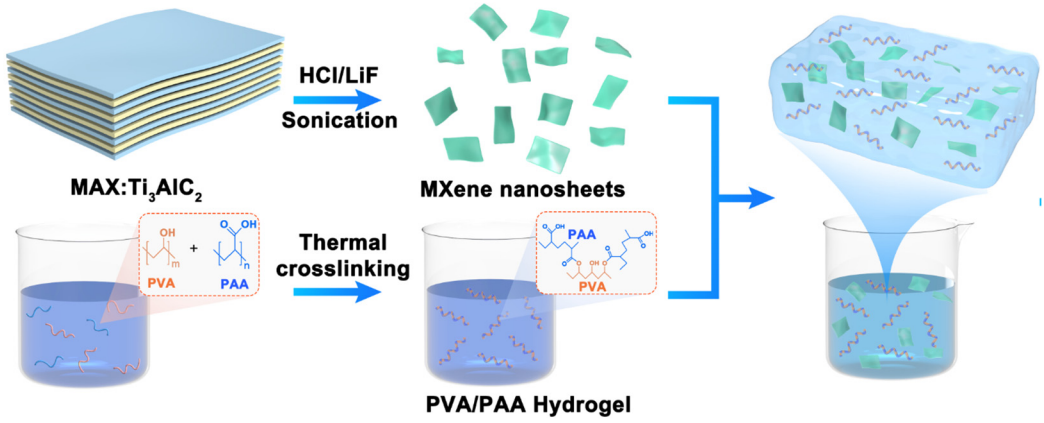

Figure 1. Steps involved in the preparation of MXene-copolymer hydrogels suitable for direct laser printing. The compositions of the formulated inks are provided in Table 1.

2.4. 3D Printing of MXene-Copolymer Hydrogels

Dogbone patterns of dimensions 100 × 6 × 5 mm following the ASTM (E8) subsize standard were modelled using Pro/ENGINEER software and exported as 'obj' files. These files were subsequently opened in Anycubic Photon Workshop 3D Slicer Software, where the following parameters were configured: z-axis movement speed of 1 mm s^{-1}, layer thickness of 50 μm, and exposure duration of 25 s per layer. For the bottom 10 layers, the exposure time was set to 30 s. The 'dl2p' format slicing file was then printed using a DLP 3D printer (Anycubic Photon D2) equipped with a near-ultraviolet (λ = 405 nm) laser. After loading the photo-responsive ink into the printer's resin tank, the defined printing program was initiated. Post-printing, the residual ink on the surface of the printed objects was gently washed off using DI water. Finally, the printed hydrogels were put into a UV curing machine (Anycubic) for 30 minutes to ensure complete curing of any uncross-linked components.

 doi:10.20944/preprints202601.0261.v1

2.5. Mechanical Property Measurement and Analysis

Tensile tests of the MXene hydrogel composites were conducted on a Shimadzu Autograph AGS-X series universal testing machine. Tensile tests were carried out at a speed of 50 mm/min, and the load and displacement data were recorded using Shimadzu Trapezium X software. Ultimate tensile strength and Young's modulus were calculated by analyzing three stress strain curves collected from each sample.

2.6. Electrochemical Response Measurement

Electrochemical response measurements were conducted on the dog-bone-shaped hydrogel composite samples by clamping the ends of each specimen with alligator clips and connecting them to a Bio-Logic SP-300 electrochemical workstation. A constant 6 V DC bias was applied throughout the measurements. Each sample was bent along its longitudinal axis from 0° to 90° in 10° increments. During each bending step, current-time traces were sampled at 0.1 s intervals, and the steady-state current was determined at each angle. For each composition (PVA-PAA, PVA-PAA-0.07MX, PVA-PAA-0.14MX, and PVA-PAA-0.28MX), angle-resolved current readings were collected across nine discrete bending angles, with 50 to 200 valid data points per angle depending on sample stability and noise level.

2.7. Machine-Learning-Assisted Current-Angle Data Analysis

Current-angle data sets obtained from the electrochemical response measurements were analyzed using Python (v3.10) with the pandas, numpy, and scikit-learn libraries. Data files were first cleaned by removing incomplete records and rounding angle values to the nearest 10°. An isotonic regression model[#] was applied to fit a monotonically increasing current-angle curve, ensuring

---

[#] *Isotonic regression model*

The sensitivity-to-noise index (SNI, units: 1/°) was defined at each bending angle θ as:

$$\mathrm{SNI}(\theta) = \frac{\left|\frac{dI}{d\theta}\right|}{\sigma(\theta)}$$

where $\left|\frac{dI}{d\theta}\right|$ is the absolute derivative of the current–angle curve and $\sigma(\theta)$ is the local noise estimated using the median absolute deviation (MAD) of residuals at angle θ. The overall SNI was computed as the mean of SNI values across interior angles (10°–80°), excluding endpoints to reduce boundary artefacts.

For inverse angle prediction, the mean absolute error (MAE) and its standard deviation (SD) were calculated across grouped cross-validation folds, where each bending angle group was held out once as the test set. For each fold k, the fold-wise MAE was defined as:

$$\mathrm{MAE_k} = \frac{1}{n_k}\sum_{i=1}^{n_k}\left|\hat{\theta}_i^{(k)} - \theta_i^{(k)}\right|$$

where $\theta_i^{(k)}$ and $\hat{\theta}_i^{(k)}$ are the true and predicted bending angles of the i-th sample in fold k, and n_k is the number of test samples in that fold.

The overall MAE and SD were then computed as:

$$\mathrm{MAE} = \frac{1}{K}\sum_{k=1}^{K}\mathrm{MAE_k}$$

 doi:10.20944/preprints202601.0261.v1

physical consistency in the directional response. At each angle, local noise was estimated using the median absolute deviation (MAD) of residuals. A sensitivity-to-noise index (SNI, units: 1/°) was computed as the absolute derivative $|dI/d\theta|$ divided by the corresponding noise $\sigma(\theta)$, and the overall SNI was reported as the mean across interior angles, excluding endpoints. To assess the accuracy of inverting current back to angle, the model was trained and evaluated using a grouped cross-validation strategy. The mean absolute error (MAE) and its standard deviation (SD) were used to quantify the model's generalization performance.

3. Results and Discussion

3.1. Structure and Properties of MXene Membranes

Prior to ink preparation, the synthesized MXene nanosheets were characterized using SEM, HRTEM and XRD. SEM characterization shows that the MXene sheets are uniform in thickness with typical lateral sizes in the 100-500 nm range (Figure S1 and S2). The structure of the MXene sheets was analyzed by XRD (Figure 2c), which shows that the (002) peak is located at 5.83°, corresponding to an interlayer spacing (*d*-spacing) of 1.52 nm according to the Bragg equation.

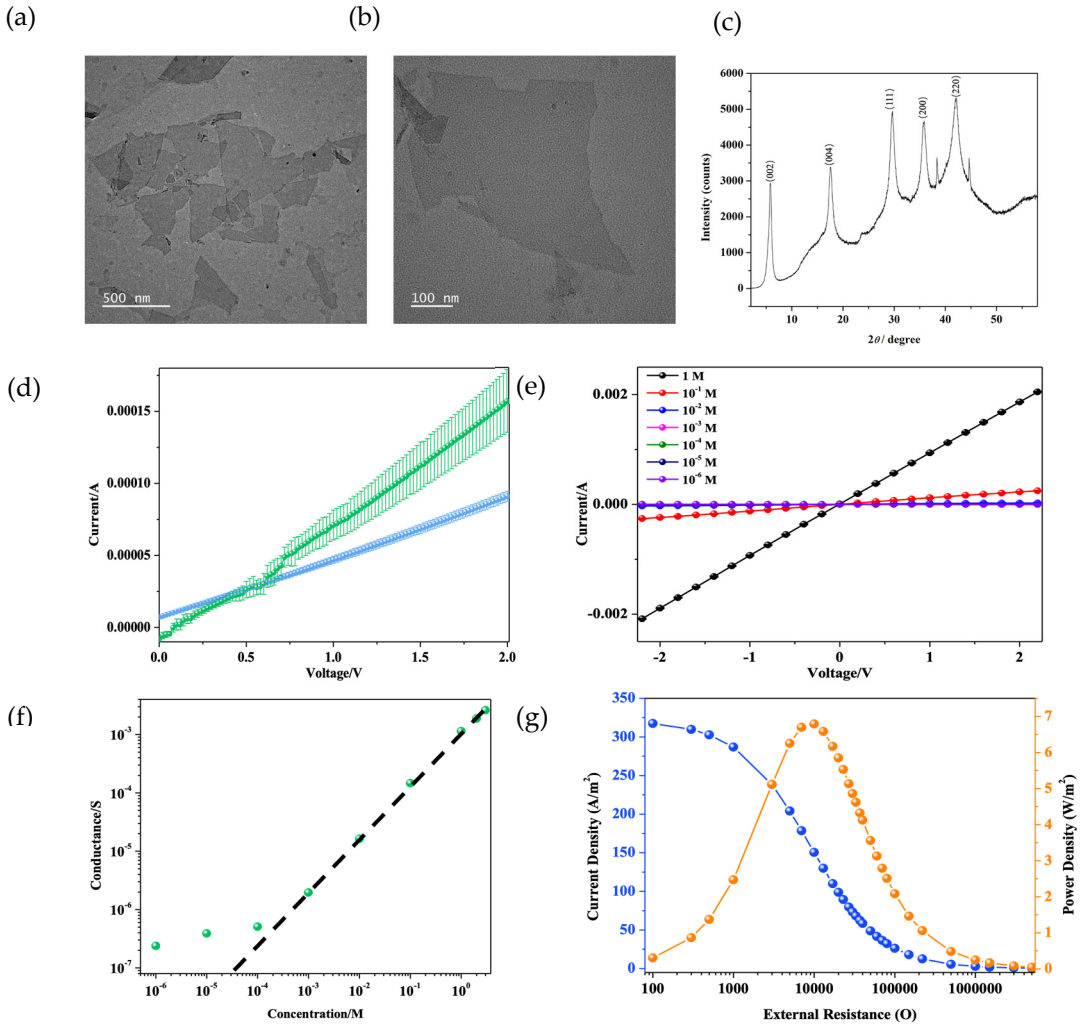

$$SD = \sqrt{\frac{1}{K-1}\sum_{k=1}^{K}(MAE_k - MAE)^2}$$

 doi:10.20944/preprints202601.0261.v1

Figure 2. Structural characterization and ion transport behaviour of synthesized MXene membranes. (a), (b) HRTEM images, (c) wide-angle XRD, (d) Ion-selective property of the MXene membrane verified by current–voltage (I-V) measurements under different gradient configurations. (e) Current versus voltage; (f) Conductance versus KCl concentration of the MXene membrane; (g) Power density and current density of MXene membranes.

3.2. Ion Transport Properties of MXene Membranes

MXene membranes are normally charged due to the F^-, O^{2-} and OH^- surface functional groups, making them perfectly suited for use in ion-selective separation[14], with applications in water treatment, gas separation, and osmotic energy conversion. When present in sufficiently high concentrations on the surfaces of lamellar MXenes, such charged surface groups induce the formation of an electrical double layer (EDL) in the channels between the MXene sheets. Due to the confinement of the double layers within the nanoscale channel volumes between neighbouring sheets, counterion transport is accelerated while co-ion transport is decelerated. There are several mechanisms by which ion-selective separation can be achieved, including size selectivity (controlled by the membrane channel or pore size),[15] charge selectivity (controlled by the charge of the diffusing ion),[16] and adsorption selectivity (controlled by the type of adsorption sites and mechanism of adsorption).[17]

The ion transport properties of the MXene membranes were investigated using current-voltage (*I-V*) measurements in a home-made electrochemical cell (Figure 2d). Measurements were conducted in KCl solutions with concentrations ranging from 10^{-4} - 2 M. These confirm that the membrane exhibited linear ohmic characteristics in a range of KCl concentrations (Figure 2e). To evaluate the ion selectivity, the MXene membrane was mounted between two electrolytes with different ion concentrations. In the absence of an external voltage (V = 0), both K^+ and Cl^- diffuse from the high (1 M) to the low (10 μM) concentration region. A net current (short-circuit current I_{sc}) is observed only when there is a difference in the diffusion rates of the two ions. Because the MXene is negatively charged, cations (*i.e.*, K^+) are enriched while anions (*i.e.*, Cl^-) are excluded from the channel, resulting in the I_{sc} direction being consistent with the positive ion flow from high to low concentration. Reversing the concentration gradient configuration results in a reversed direction of I_{sc} (Figure S4). This result demonstrates that the $Ti_3C_2T_x$ membranes exhibit a stable surface charge-controlled cation selectivity. When the ion transport from the bulk region decreased to the nanoconfined areas, the overlap of the electric double layer (EDL) calculated according to the Debye length* (λ_D) will be increased and can completely cover the pore size of the chiral layer when the concentration of the feed solution is under 0.01M (Table S1). The calculated result is in agreement with the experiment shown in Figure 2f, where the ionic conductance of the MXene is deviated from the black dash line of the 0.01 M KCl solution, which further confirms that the free-standing MXene membrane has the ability to control ion transport *via* surface charge[18]. Finally, the harvested electric power density (P_R) was assessed using the same configuration as above (Figure 2g). The power density can be calculated as $P_R = I^2 \times R_L$ with C_{MXene}/C_{silica} = 0.5/0.01 M, where R_L is the electrical loading resistance. As shown in Figure 2g, the MXene membranes can obtain 6.79 $W \bullet m^{-2}$ of osmotic energy conversion. The results confirmed that the prepared MXene membrane shows promising ability as energy conversion related device in energy storage or biomedical technology compared with other published works[14,15,19,20].

* The effective distance of the charged surface is described by the Debye length (λ_D) and can be calculated according to the equation $\lambda_D = \sqrt{\frac{\varepsilon_r \varepsilon_0 kT}{2C_{bulk} z^2 e^2}}$, where ε_r ε_0, e and k are the relatively permittivity of the solution, the permittivity of a vacuum, the electron charge, and the Boltzmann constant, respectively.

 doi:10.20944/preprints202601.0261.v1

3.3. Molecular Structure and Mechanical Properties of PAA-PVA-MXene Composites

FTIR spectroscopy within the range 4000 – 400 cm^{-1} was used to analyze the molecular structure and bonding of the MXene-hydrogel composites. Due to the low concentrations of MXene used in this work, and as observed in a prior study of low wt% MXene composites[21], there was no difference in the FTIR peaks from the freshly prepared MXene-PVA-PAA composites compared to the pure PVA-PAA sample. FTIR spectra of the freshly printed hydrogel composites (Figure 3a) clearly exhibit a broadened O-H stretching band at 3550 – 3200 cm^{-1}, indicating substantial water content as well as hydrogen bonding between PVA-PAA[22,23]. Two bands at 2952 cm^{-1} and 2922 cm^{-1} can be ascribed to C-H stretching in aliphatic CH_2 groups. Correspondingly, the C–H bending of acrylate is found at 1413 cm^{-1} and the CH_2 bending is located at 1450 cm^{-1}[24]. The characteristic C=O stretching peak of PAA presents at 1705 cm^{-1} [25–27]. A prominent band at 1635 cm^{-1} is present in the FTIR spectra of all four composites. We ascribe this band to H-O-H bending in the freshly printed hydrogel composites, as reported in previous works[25]&. The bands at low wavenumber of 1254 cm^{-1} and 1178 cm^{-1} can be attributed to C–O stretching[28] The bands located at 1090 cm^{-1} and 1050 cm^{-1} are ascribed to the P=O and P-O bonding in the light initiator LAP[29].

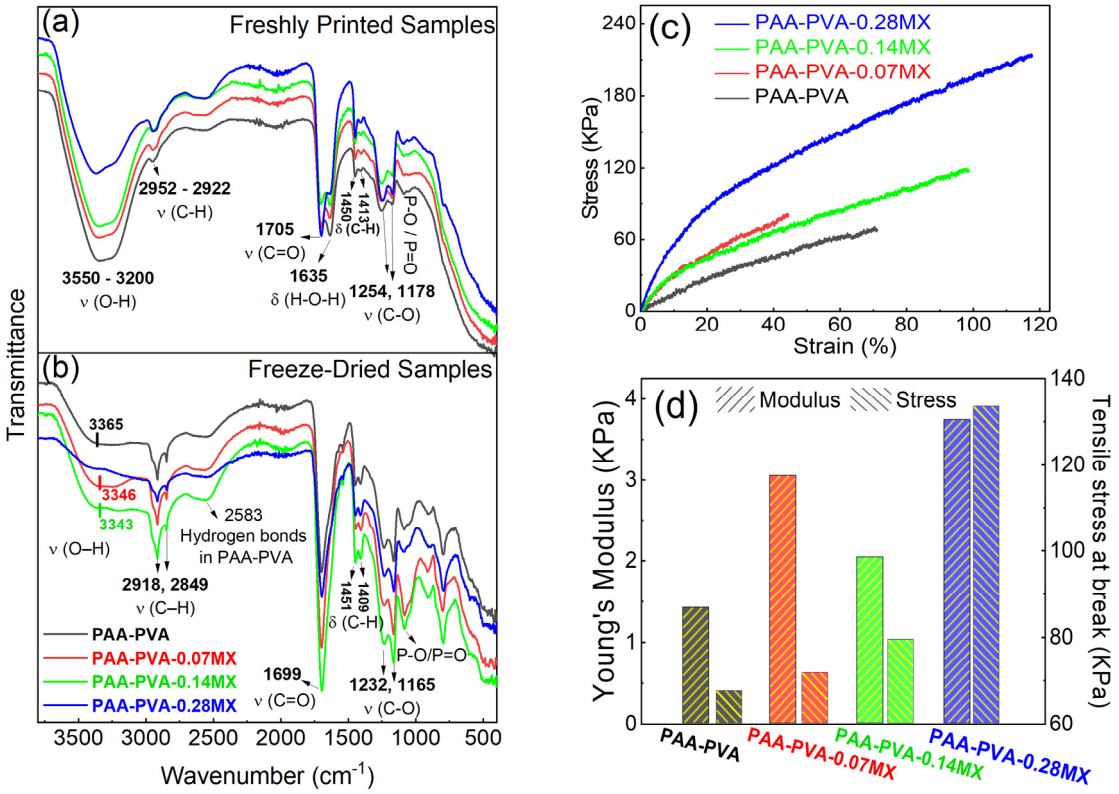

Figure 3. (a), (b) FTIR spectra of PAA/PVA-Mxene composites with 0.07-0.28 wt% MXene concentration. Vibrational mode assignments are indicated (a) before freeze drying and (b) after freeze drying. (c) Stress-strain curves of PVA-PAA hydrogel, PVA-PAA-0.07MX, PVA-PAA-0.14MX, and PVA-PAA-0.28MX composites. (d) Extracted values of Young's modulus and tensile strength.

To verify the incorporation of MXene membranes in the MXene-PVA-PAA composites, FTIR was also measured after freeze-drying (Figure 3b). The FTIR spectra of the composites exhibit sharper and more characteristic polymer bands after removing most of the free and adsorbed water. The O–H band narrows to 3400 – 3250 cm^{-1}, due to removal of water and enhancement of PVA-PAA

& The composites were extensively cured to ensure complete polymerization, ruling out assignment of this peak to the C=C bond in AA or PEGDA.

 doi:10.20944/preprints202601.0261.v1

hydrogen bonding. The O-H peak shifts from 3365 cm^{-1} for the pure PVA-PAA to 3343 cm^{-1} for the PVA-PAA-0.14MXene composite, indicating the presence of the MXene[23,25,30]. The peak at 1635 cm^{-1} that is ascribed to H-O-H bending in the freshly printed samples completely disappears and the peak at 2583 cm^{-1} due to hydrogen bonding between PVA and PAA becomes more obvious. The C=O peak shifts from 1705 cm^{-1} to 1699 cm^{-1} after freeze drying the MXene-PVA-PAA composites due to a reduction in hydrogen bonding with water and rearrangement of PAA/PEGDA carbonyl environments. The rest of the bands in the FTIR spectra of the freeze-dried MXene-PVA-PAA composites are the same as those for the freshly prepared samples.

Figure 3c displays the stress-strain curves and summarized mechanical properties of the freshly 3D printed hydrogel composites, PAA-PVA, PVA-PAA-0.07MX, PVA-PAA-0.14MX, and PVA-PAA-0.28MX. Three samples of each composite were tested using the procedure described in the Materials and Methods section. The introduction of MXene sheets into the PAA-PVA composites resulted in a progressive increase in ultimate tensile strength from 67±1 KPa at 0 wt% MXene to 71±7 KPa at 0.07 wt%, 78±26 kPa at 0.14 wt% and 133±50 KPa at 0.28 wt% as shown in Figure 3d. The increase in tensile strength may be due to the formation of strong hydrogen bonds between the MXene sheets and polyacrylic acid molecules in the PAA[31]. The Young's modulus of the composites generally increases with addition of MXene, however, the modulus of the composite with 0.07 wt% MXene is higher than at 0.14wt%.

The mechanical properties of the freshly printed hydrogel composites are summarized in Figure 3d and compared to previously reported values for similar low wt% hydrogel composites in Table 2. The study by Zhao et al., showed that at 1 wt %, the tensile strength of 3D printed PAA- MXene hydrogel were found to be 893 Kpa, substantially higher than the present work[32]. This can be ascribed to both a lower water content and higher crosslinking density due to the synthesis method in which acrylic acid (AA) monomers are pre-polymerized directly within MXene nanosheets and Ammonium Persulfate (APS) was used after 3D printing to produce a fully crosslinked hydrogel[33]. A series of GelMa-MXene composites with similar weight percentages[34] presented higher Young's modulus than our MXene-PVA-PAA composites, but much reduced strength and elongations. A starch based PAA-MXene composite displayed much better mechanical properties[25]. These differences can be attributed to differing matrices, MXene contents, manufacturing techniques, and mechanical testing conditions, and will be investigated further in the future [21,32].

Table 2. Mechanical properties of MXene PAA/PVA hydrogels (this work) compared to prior work.

MXene Composites	Manufacturing Technique	MXene wt%	Young's Modulus (KPa)	Tensile strength (KPa)	Elongation (%)
PVA-PAA-MXene (this work)	DLP 3D printing	0	1.4±0.1	67±1	65.1±6.7
		0.07	3.1± 0.1	71±7	36.2±5.2
		0.14	2.0±0.1	78±26	90.5±9.7
		0.28	3.7± 0.1	133±50	105.1±15.3
GelMa- MXene [34]	Photoinitiating solution casting	0	53.2±9.9	14±2	26.3±5.6
		0.025	45.5±4.7	11±4	26.4±3.7
		0.05	35.0±7.2	11±1	31.4±4.5
		0.125	26.01±4.3	8±2	37.3±6.6
		0.25	35.2±3.5	10±2	25.3±6.5
PAA-Starch-MXene[25]	Solution casting	0.24	211	340	1237
PAA-MXene[32]	Direct ink writing 3D printing	1	795.8	893	622

 doi:10.20944/preprints202601.0261.v1

3.4. Electrochemical Properties of 3D Printed MXene-PVA-PAA Composites

Following assessment of the osmotic energy conversion properties of the MXene membranes, MXene-PVA/PAA copolymer hydrogel inks and PVA/PAA copolymer hydrogel inks were subjected to angle-resolved electrochemical characterisation under a constant 6 V DC. Current–angle datasets were obtained across nine bending angles from 0° to 90° and served as the foundation for quantitative performance analysis. Figure 4a shows the current–angle (I–θ) responses of the 3D-printed PVA-PAA and MXene-hydrogel copolymers with MXene loadings of 0.07, 0.14, and 0.28 wt%. All samples exhibited a clear increase in electrical current with increasing bending angle across the 0–90° range. The pure PVA-PAA composite showed a quasi-linear current increase from 0.52 to 0.60 mA between 0° and 70°, followed by a sharp, non-linear increase to 0.74 mA at 90°. However, although the pure PVA-PAA hydrogel showed the largest absolute current variation, the MXene-containing composites demonstrated more uniform and linear responses throughout the full bending range. Specifically, the current increased from 0.31 to 0.37 mA for 0.07 wt%, 0.25 to 0.30 mA for 0.14 wt% and 0.06 to 0.07 mA for the 0.28 wt% MXene composite.

To quantitatively evaluate sensor performance and enable accurate angle inference from current readings, a machine-learning-assisted analysis method was implemented (Figure 4b), as described in the Materials and Methods. Figure 4c compares the overall SNI, averaged over the interior angles, for the four samples. A higher SNI value indicates superior angle sensitivity relative to noise. The PVA-PAA-0.14 wt% MXene sample achieved the highest SNI of ~4.36, indicating that a 1° change in angle produces a current response approximately 4 times greater than the background noise. This corresponds to a minimum resolvable angle of approximately 1/SNI ≈ 0.23°. The SNI values for the 0.28 wt% and 0.07 wt% samples were ~3.90 and ~3.52, respectively, while the neat PVA-PAA sample had the lowest SNI of ~1.14. This result suggests that while the pure PVA-PAA hydrogel has a larger absolute signal, its significantly higher noise level limits its effective sensitivity. We assessed the accuracy of the sensors by performing a current-to-angle inversion using 5-fold cross-validation. This process simulates the real-world application of converting a measured current back into an angle. Figure 4d shows the mean absolute angle error (MAE) of this inversion. The PVA-PAA-0.14 wt% sample demonstrated a remarkably low MAE of ≈0.0002°, significantly outperforming neat PVA-PAA (≈0.0034°), 0.07 wt% (≈0.0011°), and 0.28 wt% (≈0.0016°). Furthermore, the SD of the inversion error was also the lowest for the 0.14 wt% sample (≈0.0003°), as shown in Figure 4e and Table 3. The combination of sub-millidegree resolution and sub-microradian stability underscores the sensor's capability for highly reliable angle reconstruction and should enable applications in biomechanical monitoring such as high precision tracking of joint movements.

Table 3. Sensing performance of the PVA-PAA-MXene composites.

Name	Sensitivity to Noise (1/°)	Mean absolute angle error (°)	Standard deviation (°)
PVA-PAA	1.14	0.0034	0.003
PVA-PAA-0.07MX	3.52	0.0011	0.001
PVA-PAA-0.14MX	4.36	0.0002	0.0003
PVA-PAA-0.28MX	3.90	0.0016	0.002

 doi:10.20944/preprints202601.0261.v1

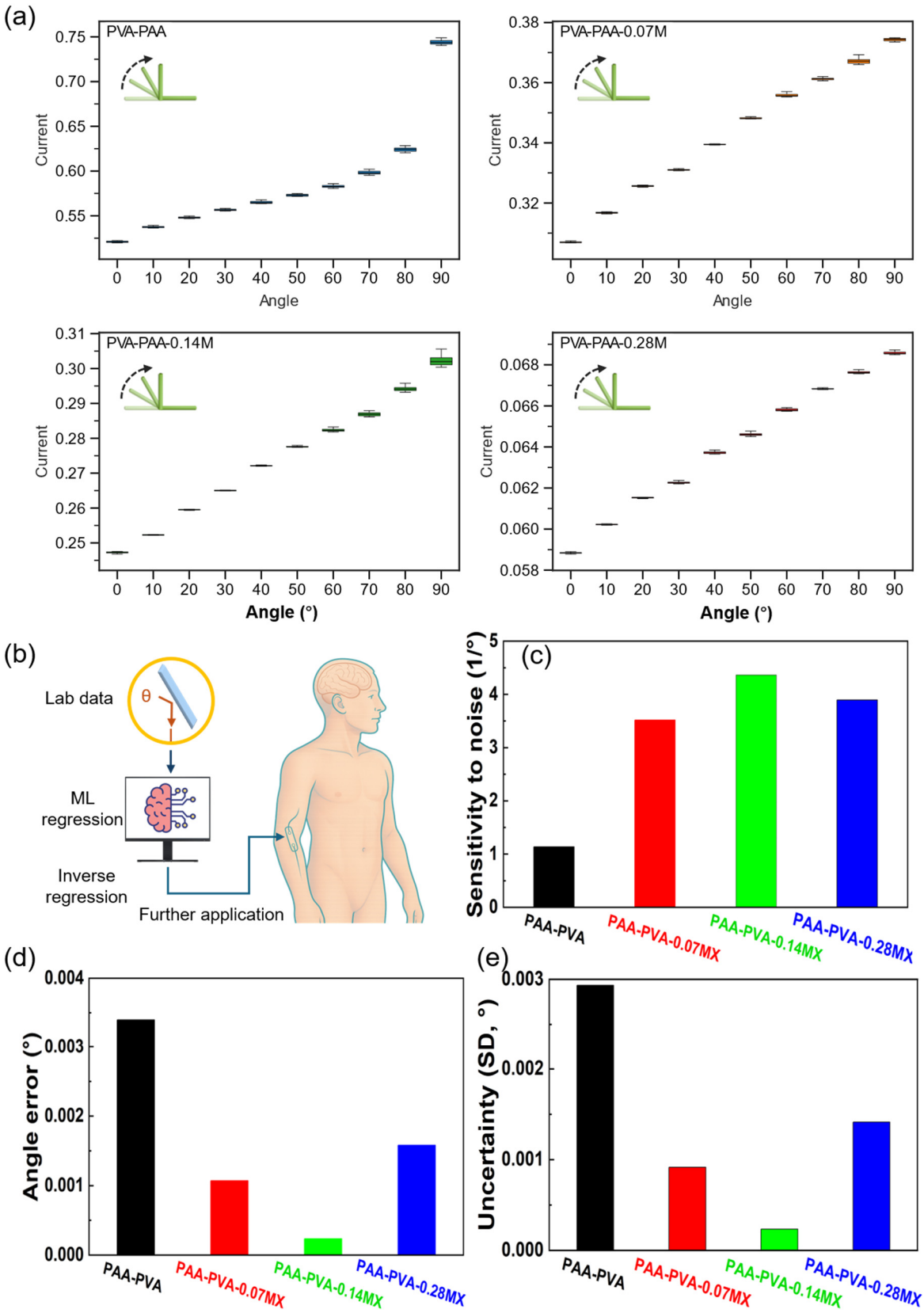

Figure 4. Electrical performance and data modelling of the 3D-printed composites: (a) Current variation during bending from 0° to 90° in 10° steps. (b) Schematic of the machine-learning-assisted analysis and an envisioned use case. (c) Comparison of the overall sensitivity metric SNI (Sensitivity-to-Noise Index, 1/°). (d) Mean absolute angle error (°) for current-to-angle inversion. (e) Standard deviation (SD, °) of the inversion error, reflecting the uncertainty in monitoring accuracy.

 doi:10.20944/preprints202601.0261.v1

4. Conclusions

We have demonstrated 3D DLP of highly flexible and biocompatible low weight % MXene-PVA-PAA composites suitable for high precision biomechanical sensing. We first synthesized the MXene nanosheets by etching the Ti_3AlC_2 MAX phase with LiF/HCl. The free-standing MXene membranes have the ability to control ion transport *via* surface charge and electrochemical measurements of harvested electric power density show 6.79 $W \bullet m^{-2}$ of osmotic energy conversion. These MXene sheets were then mixed with hydrophilic PVA-PAA polymers to formulate printable inks with MXene concentrations in the range of 0.07-0.28 wt%. DLP was used to fabricate dogbone patterned MXene-hydrogel copolymer composites which were subjected to repeated bending tests and evaluated for their performance as biomechanical sensors. The low wt% MXene-PVA-PAA composites demonstrate high mechanical flexibility and high precision for sensing acute bending angles. Further work will focus on improving the mechanical properties (Young's modulus and tensile strengths) while retaining the electromechanical sensing performance and evaluating performance in real-world biomechanical applications such as high precision tracking of joint movements.:

Supplementary Materials: The following supporting information can be downloaded at the website of this paper posted on Preprints.org.

Authors' contributions: E. Alghamdi conducted mechanical testing and FTIR experiments; C. Lobo and H. Xu analyzed mechanical testing and FTIR experiments; S.Mao prepared the MXene-hydrogel copolymers; S. Mao and Q. Fu conducted 3D printing; H. Xu and B. Sun conducted electrochemical characterisation; T. Huang conducted maching learning analysis; Y. Huang synthesized the MXene membranes; N. Xu and Y. Huang conducted SEM characterization and osmotic energy conversion experiments; and C. Lobo, H. Xu and Y. Huang conceived and designed the study and wrote the manuscript. All authors contributed to the Figures.

Financial support and sponsorship: This work was supported by UTS Cross-faculty grant PRO22-15132 and National Natural Science Foundation of China grant (22308127).

Availability of data and materials: Supporting information detailing structural and chemical characterization of the synthesised materials, and osmotic energy conversion measurements, is provided online.

Acknowledgments: The authors thank Xin Guo and Hao Liu for assistance with $Ti_3C_2T_x$ exfoliation.

Conflicts: of interest: The authors declare no conflicts of interest.

References

1. Liu, Y. C.; Zhang, S. P.; Song, R. Y.; Zeng, H. O.; Wang, L. D. Preanchoring Enabled Directional Modification of Atomically Thin Membrane for High-Performance Osmotic Energy Generation. *Nano Lett.* **2023**, *24* (1), 26-34, Article. DOI: 10.1021/acs.nanolett.3c03041.
2. Hafa, L.; Breideband, L.; Posada, L. R.; Torras, N.; Martinez, E.; Stelzer, E. H. K.; Pampaloni, F. Light Sheet-Based Laser Patterning Bioprinting Produces Long-Term Viable Full-Thickness Skin Constructs. *ADVANCED MATERIALS* **2024**, *36* (8). DOI: 10.1002/adma.202306258.
3. Sanchis-Gual, R.; Ye, H.; Ueno, T.; Landers, F. C.; Hertle, L.; Deng, S. Y.; Veciana, A.; Xia, Y. M.; Franco, C.; Choi, H.; et al. 3D Printed Template-Assisted Casting of Biocompatible Polyvinyl Alcohol-Based Soft Microswimmers with Tunable Stability. *Adv. Funct. Mater.* **2023**, *33* (39). DOI: 10.1002/adfm.202212952.
4. Zheng, B. J. D.; Zhao, G.; Yan, Z.; Xie, Y. C.; Lin, J. Direct Freeform Laser Fabrication of 3D Conformable Electronics. *Adv. Funct. Mater.* **2023**, *33* (1). DOI: 10.1002/adfm.202210084.
5. Gogotsi, Y.; Anasori, B. The Rise of MXenes. *ACS Nano* **2019**, *13* (8), 8491-8494. DOI: 10.1021/acsnano.9b06394.
6. Mahmud, M. A. P.; Huda, N.; Farjana, S. H.; Asadnia, M.; Lang, C. Recent Advances in Nanogenerator-Driven Self-Powered Implantable Biomedical Devices. *Adv. Energy Mater.* **2018**, *8* (2), 25, Review. DOI: 10.1002/aenm.201701210.

 doi:10.20944/preprints202601.0261.v1

7. Tsang, A. C. H.; Zhang, J. T.; Hui, K. N.; Hui, K. S.; Huang, H. B. Recent Development and Applications of Advanced Materials via Direct Ink Writing. *Adv. Mater. Technol.* **2022**, *7* (7). DOI: 10.1002/admt.202101358.
8. Yang, G. Y.; Sun, Y. Y.; Qin, L. M.; Li, M. R.; Ou, K. T.; Fang, J.; Fu, Q. Direct-ink-writing (DIW) 3D printing functional composite materials based on supra-molecular interaction. *Compos. Sci. Technol.* **2021**, *215*. DOI: 10.1016/j.compscitech.2021.109013.
9. Li, L. L.; Deng, Z. M.; Chen, M. J.; Yu, Z. Z.; Russell, T. P.; Zhang, H. B. 3D Printing of Ultralow-Concentration 2D Nanomaterial Inks for Multifunctional Architectures. *Nano Lett.* **2023**, *23* (1), 155-162, Article. DOI: 10.1021/acs.nanolett.2c03821.
10. McLellan, K.; Li, T. R.; Sun, Y. C.; Jakubinek, M. B.; Naguib, H. E. 4D Printing of MXene Composites for Deployable Actuating Structures. *ACS APPLIED POLYMER MATERIALS* **2022**, *4* (12), 8774-8785. DOI: 10.1021/acsapm.2c01192.
11. Jambhulkar, S.; Liu, S. Y.; Vala, P.; Xu, W. H.; Ravichandran, D.; Zhu, Y. X.; Bi, K.; Nian, Q.; Chen, X. F.; Song, K. N. Aligned Ti₃C₂T_x MXene for 3D Micropatterning via Additive Manufacturing. *ACS Nano* **2021**, *15* (7), 12057-12068, Article. DOI: 10.1021/acsnano.1c03388.
12. Jiang, P. Z.; Deng, Z. M.; Min, P.; Ye, L. X.; Qi, C. Z.; Zhao, H. Y.; Liu, J.; Zhang, H. B.; Yu, Z. Z. Direct ink writing of multifunctional gratings with gel-like MXene/norepinephrine ink for dynamic electromagnetic interference shielding and patterned Joule heating. *Nano Res.* **2024**, *17* (3), 1585-1594, Article. DOI: 10.1007/s12274-023-6044-9.
13. Chen, X. Y.; Zhao, Y. Y.; Li, L. Z.; Wang, Y. H.; Wang, J. L.; Xiong, J. J.; Du, S. L.; Zhang, P.; Shi, X. R.; Yu, J. H. MXene/Polymer Nanocomposites: Preparation, Properties, and Applications. *Polym. Rev.* **2021**, *61* (1), 80-115, Review. DOI: 10.1080/15583724.2020.1729179.
14. Hong, S. H. Y.; Al Marzooqi, F.; El-Demellawi, J. K.; Al Marzooqi, N.; Arafat, H. A.; Alshareef, H. N. Ion-Selective Separation Using MXene-Based Membranes: A Review. *ACS Mater. Lett.* **2023**, *5* (2), 341-356, Review. DOI: 10.1021/acsmaterialslett.2c00914.
15. Zhou, S.; Xie, L.; Li, X.; Huang, Y.; Zhang, L.; Liang, Q.; Yan, M.; Zeng, J.; Qiu, B.; Liu, T.; et al. Interfacial Super-Assembly of Ordered Mesoporous Carbon-Silica/AAO Hybrid Membrane with Enhanced Permselectivity for Temperature- and pH-Sensitive Smart Ion Transport. *Angewandte Chemie International Edition* **2021**, *60* (50), 26167-26176. DOI: https://doi.org/10.1002/anie.202110731 (acccessed 2025/10/09).
16. Huang, Y.; Zeng, H.; Xie, L.; Gao, R.; Zhou, S.; Liang, Q.; Zhang, X.; Liang, K.; Jiang, L.; Kong, B. Super-Assembled Chiral Mesostructured Heteromembranes for Smart and Sensitive Couple-Accelerated Enantioseparation. *Journal of the American Chemical Society* **2022**, *144* (30), 13794-13805. DOI: 10.1021/jacs.2c04862.
17. Huang, Y.; Liang, Q.; Yin, H.; Zhang, X.; Gao, R.; Pan, J.; Liang, K.; Jiang, L.; Kong, B. pH Modulation of Super-Assembled Heteromembranes for Sustainable Chiral Sensing. *ACS Nano* **2024**, *18* (19), 12547-12559. DOI: 10.1021/acsnano.4c02720.
18. Huang, Y. N.; Liang, Q. R.; Yin, H. B.; Zhang, X.; Gao, R. H.; Pan, J. M.; Liang, K.; Jiang, L.; Kong, B. pH Modulation of Super-Assembled Heteromembranes for Sustainable Chiral Sensing. *ACS Nano* **2024**, *18* (19), 12547-12559. DOI: 10.1021/acsnano.4c02720.
19. Huang, Y. A.; Zeng, H.; Xie, L.; Gao, R. H.; Zhou, S.; Liang, Q. R.; Zhang, X.; Liang, K.; Jiang, L.; Kong, B. Super-Assembled Chiral Mesostructured Heteromembranes for Smart and Sensitive Couple-Accelerated Enantioseparation. *JOURNAL OF THE AMERICAN CHEMICAL SOCIETY* **2022**, *144* (30), 13794-13805. DOI: 10.1021/jacs.2c04862.
20. Xie, L.; Zhou, S.; Liu, J.; Qiu, B.; Liu, T.; Liang, Q.; Zheng, X.; Li, B.; Zeng, J.; Yan, M.; et al. Sequential Superassembly of Nanofiber Arrays to Carbonaceous Ordered Mesoporous Nanowires and Their Heterostructure Membranes for Osmotic Energy Conversion. *Journal of the American Chemical Society* **2021**, *143* (18), 6922-6932. DOI: 10.1021/jacs.1c00547.
21. Srinivas, P.; Jacob, L.; C, S. M.; Butt, H.; Barsoum, I.; Al-Rub, A. K. R.; Zaki, W. Mechanical Properties, Energy Absorption, and Shape Memory Behavior of 3D Printed PLA-MXene Nanocomposites and Gyroid Lattices. *Advanced Engineering Materials* **2024**, *26* (12). DOI: 10.1002/adem.202301698.

22. Gong, S.; Sheng, X.; Li, X.; Sheng, M.; Wu, H.; Lu, X.; Qu, J. A Multifunctional Flexible Composite Film with Excellent Multi-Source Driven Thermal Management, Electromagnetic Interference Shielding, and Fire Safety Performance, Inspired by a "Brick–Mortar" Sandwich Structure. *Adv. Funct. Mater.* **2022**, *32* (26), 2200570. DOI: https://doi.org/10.1002/adfm.202200570.
23. Kim, J.; Choi, Y.; Jang, H.; Jiong, S.; Chen, X.; Seo, B.; Choi, W. Thermo-Chemo-Mechanically Robust, Multifunctional MXene/PVA/PAA-Hanji Textile with Energy Harvesting, EMI Shielding, Flame-Retardant, and Joule Heating Capabilities. *Advanced Materials* **2024**, *36* (47), 2411248. DOI: https://doi.org/10.1002/adma.202411248.
24. Fahmy, A.; Eisa, W. H.; Yosef, M.; Hassan, A. Ultra-Thin Films of Poly(acrylic acid)/Silver Nanocomposite Coatings for Antimicrobial Applications. *Journal of Spectroscopy* **2016**, *2016* (1), 7489536. DOI: https://doi.org/10.1155/2016/7489536.
25. Liang, J.; Ma, K.; Gao, W.; Xin, Y.; Chen, S.; Qiu, W.; Shen, G.; He, X. Enhanced mechanical and electrical properties of starch-based hydrogels incorporating polyacrylic acid and MXene for advanced wearable sensors in sign language recognition. *Sensors & Diagnostics* **2024**, *3* (2), 256-268, 10.1039/D3SD00250K. DOI: 10.1039/D3SD00250K.
26. Bai, Y.; Lu, Y.; Bi, S.; Wang, W.; Lin, F.; Zhu, F.; Yang, P.; Ding, N.; Liu, S.; Zhao, W.; et al. Stretchable and Photothermal MXene/PAA Hydrogel in Strain Sensor for Wearable Human-Machine Interaction Electronics. *Adv. Mater. Technol.* **2023**, *8* (9), 2201767. DOI: https://doi.org/10.1002/admt.202201767.
27. Ding, N.; Bai, Y.; Feng, Y.; Zou, X.; Chen, Y.; Bi, S.; Liu, S.; Zhao, W.; Zhao, Q. Multifunctional MXene/PAA organohydrogel as a flexible strain sensor for wearable human–machine interaction. *RSC Applied Polymers* **2023**, *1* (1), 64-72, 10.1039/D3LP00052D. DOI: 10.1039/D3LP00052D.
28. Mansur, H. S.; Sadahira, C. M.; Souza, A. N.; Mansur, A. A. P. FTIR spectroscopy characterization of poly (vinyl alcohol) hydrogel with different hydrolysis degree and chemically crosslinked with glutaraldehyde. *Materials Science and Engineering: C* **2008**, *28* (4), 539-548. DOI: https://doi.org/10.1016/j.msec.2007.10.088.
29. Jastrzębski, W.; Sitarz, M.; Rokita, M.; Bułat, K. Infrared spectroscopy of different phosphates structures. *Spectrochimica Acta Part A: Molecular and Biomolecular Spectroscopy* **2011**, *79* (4), 722-727. DOI: https://doi.org/10.1016/j.saa.2010.08.044.
30. Jin, C.; Bai, Z. MXene-Based Textile Sensors for Wearable Applications. *ACS Sensors* **2022**, *7* (4), 929-950. DOI: 10.1021/acssensors.2c00097.
31. Bai, W.; Yong, Z.; Wang, S.; Wang, X.; Li, C.; Pan, F.; Liang, D.; Cui, Y.; Wang, Z. Polyaniline-MXene composite electrode with excellent electrochemical properties for all-solid flexible supercapacitors. *Journal of Energy Storage* **2023**, *71*, 108053. DOI: 10.1016/j.est.2023.108053.
32. Zhao, W.; Cao, J.; Wang, F.; Tian, F.; Zheng, W.; Bao, Y.; Zhang, K.; Zhang, Z.; Yu, J.; Xu, J.; et al. 3D Printing of Stretchable, Adhesive and Conductive Ti3 C2 Tx-Polyacrylic Acid Hydrogels. *Polymers* **2022**, *14* (10). DOI: 10.3390/polym14101992.
33. Zhao, W.; Cao, J.; Wang, F.; Tian, F.; Zheng, W.; Bao, Y.; Zhang, K.; Zhang, Z.; Yu, J.; Xu, J.; et al. 3D Printing of Stretchable, Adhesive and Conductive Ti3C2Tx-Polyacrylic Acid Hydrogels. *Polymers* **2022**, *14* (10), 1992. DOI: 10.3390/polym14101992.
34. Lotfi, R.; Dolatyar, B.; Zandi, N.; Tamjid, E.; Pourjavadi, A.; Simchi, A. Electrically conductive and photocurable MXene-modulated hydrogel conduits for peripheral nerve regeneration: In vitro and in vivo studies. *Biomaterials Advances* **2025**, *170*, 214197. DOI: 10.1016/j.bioadv.2025.214197.